Influence of milling on structural and microstructural properties of cerium oxide: Consequence of the surface activation on the dissolution kinetics in nitric acid

Julia Hidalgo, Pascal Roussel, Hanako Okuno, Thibaud Delahaye, Jean Luc Rouvière, Gilles Leturcq

Influence of milling on structural and microstructural properties of cerium oxide: Consequence of the surface activation on the dissolution kinetics in nitric acid

Julia Hidalgo, Pascal Roussel, Hanako Okuno, Thibaud Delahaye, Jean Luc Rouviere, Gilles Leturcq

PII: S0304-386X(21)00223-1

DOI: https://doi.org/10.1016/j.hydromet.2021.105774

Reference: HYDROM 105774

To appear in: *Hydrometallurgy*

Received date: 4 January 2021

Revised date: 26 October 2021

Accepted date: 30 October 2021

Please cite this article as: J. Hidalgo, P. Roussel, H. Okuno, et al., Influence of milling on structural and microstructural properties of cerium oxide: Consequence of the surface activation on the dissolution kinetics in nitric acid, *Hydrometallurgy* (2021), https://doi.org/10.1016/j.hydromet.2021.105774

Influence of milling on structural and microstructural properties of cerium oxide: consequence of the surface activation on the dissolution kinetics in nitric acid

Julia Hidalgo[1], Pascal Roussel[2], Hanako Okuno[3], Thibaud Delahaye [1], Jean Luc Rouviere[3], Gilles Leturcq[1,*] gilles.leturcq@cea.fr
[1]CEA, DES, ISEC, University of Montpellier, Marcoule, France
[2]Univ. Lille, CNRS, Centrale Lille, Univ. Artois, UMR 8181 - UCCS - Unité de Catalyse et Chimie du Solide, F-59000 Lille, France
[3]Univ. Grenoble Alpes, CEA, IRIG-MEM, LEMMA, 17 rue des martyrs, F-38000 Grenoble, France
[*]Corresponding author.

Abstract
Ceria (CeO_2) is known as a refractory oxide for dissolution in nitric acid since the leaching reaction is thermodynamically unfavorable, except when it is complexed by nitrates but with very slow kinetics. To enhance dissolution, surface activation was achieved using high-energy milling. With the mechanically-activated cerium oxide, leaching in nitric acid reached 36%. The mechanical activation of the solid caused structural and microstructural changes (particle size, specific surface area, crystallite size, lattice strain, defects…). After one hour, the cleavage induced by energetic milling generated two populations: nanoparticles and grains containing defects like dislocations. Beside crystallite size and micro-strain evaluation using X-ray diffraction, cerium oxidation state was measured by Electron Energy-Loss Spectroscopy (EELS) analyses while linear defects were pictured by Transmission Electron Microscopy (TEM) observations. On one hand, it was found that the nanoparticles formed during milling process greatly enhance the dissolution reaction by the creation of Ce^{3+} thin layers of a few nanometer depth on their surfaces. On the other hand, it is shown that dislocations represent another way to increase the kinetics by activation energy. In conclusion, dissolution rate's growth can be due to different parameters like the leaching of the smallest particles, the presence of reduced oxidation state on nanoparticles and some highly reactive sites concentrating structural defects such as dislocation nodes. Finally, as ceria is also well known to be a safe analogue of PuO_2, especially for dissolution studies, a solution for improving the dissolution of ceria would probably also be useful for dissolving the oxides rich in Pu.

Keywords: Cerium oxide / Milling / Dissolution / Oxygen vacancy / Dislocation / Strain

1. Introduction

Currently 96% of spent nuclear UO_x fuel is composed of U (95%) and Pu (1%) being valorized as uranium and plutonium mixed oxide fuel (called MOX). In order to recycle these two valuable elements, spent fuels are treated by the PUREX (Plutonium Uranium Reduction Extraction) process (Poinssot et al., 2012; Taylor, 2015). This process is currently used in the reprocessing plants and is composed by different steps such as shearing fuel rods, dissolving spent fuel in nitric acid and extracting valuable chemical elements. The purified Pu is then recycled once through LWR (Light-Water Reactor) MOX fuels with Pu content of less than 10 wt%.

Subsequently, it is planned to develop generation IV, fast reactors (FR) for the multi-recycling of plutonium. This fuel is composed of depleted uranium and plutonium at 20-30 wt%. Recycling processes should take into account the increase in Pu content in future spent nuclear fuels (1% UOX, <10% LWR MOX and up to 30% FR fuel) (Touron et al., 2016). If spent UOx fuel is easily dissolved in nitric acid, dissolution of spent MOX fuel is more difficult due to the presence of Pu-rich clusters. Indeed $U_{1-x}Pu_xO_2$ phases with x higher than 0.3 almost stays undissolved after 6 h in concentrated nitric acid (Vollath et al.,

1985). Therefore, considering spent FR MOX treatment, simple nitric dissolution would end up with Pu rich residues that would have to be recovered to prevent any criticality accident. Complementary treatments for these dissolution residues are under development in order to keep a Pu recovery yield of 99.9% as it is for UOX fuels (Brueziere et al., 2013). These Pu based residues being strongly resistant to corrosion in conventional nitric acid media, many studies were devoted to optimize chemical conditions of the attack conditions. Improvement of dissolution kinetics require an hardening of these chemical conditions by modifying the main dissolution parameters such as acidity (Goode, 1965; Uriarte and Rainey, 1965), temperature (Fournier, 2000) and addition of complexing agent (Katz et al., 1987; Scott Barney, 1977). One option is to use nitric and hydrofluoric acid mixtures at boiling temperature under reflux (Scott Barney, 1977). However, the kinetics of reaction is very slow for high temperature treated oxides with low specific surface area (less than 1 $m^2\ g^{-1}$) and solutions are highly corrosive which raises reactor corrosion issues. These conditions induce some problems for the following steps of PUREX process. Another option, currently used in La Hague, ORANO plant for dissolving non-compliant PuO_2, requires a low content of electroregenerated Ag(II). This ion allows the oxidation of Pu(IV) to Pu(VI) enhancing dissolution kinetics (Bourges et al., 1986).

Another possibility to improve oxides dissolution kinetics is the enhancement of solid reactivity by an increase of specific surface area and the formation of energetically reactive sites (Blum et al., 1990; Corkhill et al., 2014; Tromans and Meech, 1999) like oxygen vacancies and linear defects. Some studies in literature report that higher dissolution kinetics correspond to materials having the smallest crystallite sizes and thus the highest specific surface areas (Claparede et al., 2015). The role of preferentially attacked sites with high surface energy on the initial dissolution rate is also mentioned in the literature for ceramic materials (Albanese-Kotar and Mikkola, 1987). Mechanical activation, usually done by high-energy milling, is considered as an alternative route to current processes. Milling show significant acceleration of dissolution processes due to the generation of structural defects, being high-energy reaction sites and catalyze dissolution reactions (Baláž et al., 1996; Blum and Lasaga, 1988; Tkáčová et al., 1993).

Ceria is frequently used as a surrogate for plutonium dioxide, their similitudes are detailed and compared in next paragraph. Both materials are resistant to hydrometallurgical dissolution processes. Therefore, a solution for improving the dissolution of ceria would probably also be useful for dissolving the oxides rich in Pu. Moreover, due to several properties of interest such as UV absorbing ability (Tsunekawa et al., 2000), high thermal stability (Trovarelli et al., 1999), high hardness (Chen and Chang, 2005), ability to store and transport oxygen (Hull et al., 2009; Kim et al., 2008; Paier et al., 2013), and possibility for cerium to change its oxidation state between Ce(+III) and Ce (+IV) (Hull et al., 2009; Skorodumova et al., 2002), ceria has been exploited since the 1980s for several applications including catalysis (Trovarelli, 2002), optical additive (Goharshadi et al., 2011; Tsunekawa et al., 1999), and ionic conduction (Park et al., 2000). As this material is now widely used, dissolution could represent the first step in its recycling.

Several studies deal with the modelling of ceria dissolution. The effect of microstructural properties of CeO_2 on its dissolution in nitric acid 8.5 M at 95°C was modeled only with two variables: crystallite size (Tc in nm) and specific surface area (SSA in $m^2\ g^{-1}$), r being the dissolution kinetics in % dissolved min^{-1} (Ziouane et al., 2018):

$$r = k \times Tc^{-1} \times SSA^{0.33} \qquad \text{(Equation 1)}$$

Another model was established as a function of several defects identified in ceramic oxides in case of dissolutions in nitric acid medium at 90°C (Corkhill et al., 2016),

$$\mathrm{C_{Ce}} = \frac{SSA}{SSA_0}\left[\alpha A_3\left(1 - e^{-b_3 t}\right) + (1 - \alpha)A_4(1 - e^{-b_4 t}\right] \qquad \text{(Equation 2)}$$

where C_{Ce} is the concentration of Ce, SSA ($m^2\ g^{-1}$) is the measured specific surface area (after dissolution in the case of CeO_{2-x}), SSA_0 is a reference specific surface area of 1 $m^2\ g^{-1}$, α is the fraction of Ce^{3+} (representing the oxygen vacancy content determined by XPS), A_3 and A_4 correspond to the solubility limits of Ce^{3+} and Ce^{4+} respectively, and b_3 and b_4 are the rate constants for Ce^{3+} and Ce^{4+}.

The highest CeO_2 dissolution rate was observed for the sample exhibiting greater amounts of high-energy surface sites, intrinsic defects and oxygen vacancies. Dissolution of these oxygen vacancy sites in CeO_{2-x} is greatly increased due to the presence of Ce^{3+}. The greater solubility of Ce^{3+} influenced the dissolution rate compared to Ce^{4+} in CeO_2 like those calcined at high temperatures. Moreover, oxygen vacancy ratio change the lattice volume and constrains the crystalline structure. Dissolution improves by stress relaxation induced by lattice strain. Introduction of trivalent element inside the ceria structure leads to both the creation of oxygen vacancies and to an increase strain in lattice. Such addition creates oxygen vacancies and constrains the crystal lattice resulting in a higher dissolution rate. Some articles deal with the incorporation of trivalent lanthanides (La, Nd, Sm, Gd, Dy, Er, Yb) to create oxygen vacancies and modify solid properties in order to promote dissolution (Horlait et al., 2012, 2014). It was shown that samples doped with trivalent elements are more efficiently dissolved. Other authors have optimized chemical media, with sonochemical method, involving platinum nanoparticle deposit on the cerium oxide and the addition of ascorbic acid to initiate a reductive dissolution (Beaudoux et al., 2016a).

The present work describes the effect of grinding on CeO_2's structure and microstructure. The influence of these modifications on dissolution is investigated. To understand these effects, kinetics and mechanism of cerium oxide dissolution are examined by comparing activated samples with un-ground samples exhibiting equivalent microstructural properties.

2. ***Experimental details***

2.1 CeO_2 surrogate of PuO_2

Ceria is used as a surrogate for PuO_2 since both oxides crystallize in the same fluorite-type structure (FCC, Fm-3m, PDF cards 03-065-2975 for CeO_2 and 00-051-0798 for PuO_2) with equivalent ionic radius (Ce^{4+}=0.97 Å and Pu^{4+}=0.96 Å).

With similar free energies of dissolution (ΔrG_{Ce}^0 = 40 kJ mol^{-1} for cerium oxide and ΔrG_{Pu}^0 = 41 kJ mol^{-1} for plutonium oxide (Joret, 1995), the dissolution of these oxides is not thermodynamically favorable. Ziouane et al.(2018) studied the dissolution of PuO_2 and CeO_2 as a function of structural parameters (initial micro strain, crystallite size) and microstructural (specific surface area, particle size, morphology) depending on the conditions of production (synthesis route, calcination temperature) and conditions of dissolution (acidity, temperature). Like cerium dioxide, plutonium dioxide is refractory to dissolution in a nitric medium. Aggressive dissolution conditions must be used to significantly improve kinetics. The dissolution of these two oxides follows the same model. This model depends on the nature of the oxide, the structural and microstructural parameters and environmental conditions. By maintaining the attack conditions (at 8.5 M HNO_3 and 95°C) and parameters constant, the authors demonstrated that the kinetic constant of CeO_2 is only 3 times greater than that of PuO_2. This validates the use of CeO_2 to simulate the behavior of PuO_2 on dissolution. Reducing dissolution (reductive leaching) can also be applied to both oxides in order to enhance dissolution rates (Dalodiere et al., 2017 ; Beaudoux et al., 2016b).

2.2 Oxide syntheses

High purity (>99.9%) Sigma-Aldrich commercial reagents were used for this study. Two different routes were performed in order to synthetize CeO_2 powder with different microstructural proprieties. In a first step, two CeO_2 batches were obtained by thermal conversion of oxalate precursors precipitated in excess of oxalic acid from cerium nitrate solutions. The oxalic conversion is usually reported to synthetize actinide

oxides (Burney and Smith, 1984; Rankin and Burney, 1975). Cerium nitrate hexahydrate was dissolved in water. The cerium precipitate was obtained by mixing this solution containing Ce(III) with oxalic acid as complexing agent solution. Concentrations of these solutions were fixed in order to reach in the precipitator a final concentration of nitric acid equal to 1 mol L^{-1} and an oxalic excess of 0.20 mol L^{-1}. Oxalic precipitation of trivalent cerium leads to an oxalate with $Ce_2(C_2O_4)_3 \cdot 10H_2O$ formula (Agarwala and Naik, 1961; De Almeida et al., 2012; Heintz and Bernier, 1986). The solid obtained by this route presents a monoclinic structure and crystallized in the form of platelet agglomerates. The precipitate was filtered and rinsed with deionized water before being air-dried. To obtain oxides with different microstructural properties, this precursor was split onto two batches before being calcined under air atmosphere at 1200°C and 600°C, respectively, with a heating rate of 5°C min^{-1} and the final temperature maintained for 2 hours before cooling down to room temperature. The aim of the use of different calcination temperatures is the obtention of two oxides with different microstructural properties.

In a second step, a batch of ceria was obtained using Nitrate Poly-acrylate Gel (NPG) method in the presence of Poly(ethylene glycol)-block-poly(propylene glycol)-block-poly(ethylene glycol) (P123). Cerium nitrate ($Ce(NO_3)_3$) was dissolved in nitric acid. The P123 compound was dissolved in the cerium solution. Then, this solution was added to acrylic acid (AA) and N, N′-methylene bis (acrylamide) (MBAM). The resulting homogeneous solution was heated up to 100°C. A sample of 25 µL of Hydrogen peroxide (1.6 M) and ascorbic acid (0.8 M) were quickly incorporated to initiate the complete polymerization of the solution to form a gel. This gel was finally dried at 150°C to form a xerogel, which was converted in oxide through an oxidative calcination at 600°C in air for 2 h. During this treatment, the total oxidation of all residual carbon compounds takes place, leading to the synthesis of oxide (Leblanc et al., 2019). This NPG method was used since it is known for the development of a process for the synthesis of actinide or lanthanide oxide on a smaller scale. The advantage of this method is that it allows a low production of liquid effluents, thus increasing the compactness of the process.

2.3 Milling procedure

A ball miller (Mirco-serie from NETZCH) with a rotation speed of 4200 revolutions min^{-1} was used in the mechanical activation test of CeO_2. The reaction chamber was about 60 mL and balls used were 0.6 mm (zirconium oxide) in diameter and represent 85% of total volume. The ceria mass to water volume ratio was 1:250 (g mL^{-1}) for the milling operation. Ball-milling duration lasted for 60 min with a gross power input of 0.84 kW. The suspension containing water and ground cerium was circulated using a peristaltic pump with a flow rate of 110 mL min^{-1}. Suspension was finally dried in a ventilated oven at 80°C to allow the recovery of the solid before characterizations.

2.4 Dissolution procedure

The dissolution procedure consisted in suspending 300 mg of oxide powder in 15 mL of nitric acid solution. The experiments were carried out at a temperature of 95°C with the presence of a magnetic stirrer in the reactor (stirring at ~400 rpm). Regular sampling of the dissolution liquor (0.5 mL) were sampled, filtered on PTFE (polytetrafluoroethylene) filters (0.2 µm, VWR), and diluted with deionized water and HNO_3. Only a part of the sample (0.2 mL of the 0.5 mL) was analyzed using ICP-AES (for Inductively coupled plasma atomic emission spectroscopy) device (Horiba Jobin Yvon from Activa), after a dilution in order to keep a constant nitric acidity of 0.5 M and a cation concentration range from 0.1 to 10 mg/L(ppm). External calibration curves were prepared with certified Ce and Zr standard solutions of 1000 mg/L (SCP Science). The error on each value depends on the law of uncertainty propagation, which considers dilution uncertainties, measurement errors, calibration and the device error. It can be expressed by the square root of the sum of the squares of the uncertainties. Uncertainties on mass of powder, volume of aliquot,

dilution and ICP-AES measurements were taken into account. Dissolution advancement is given as percentage of cerium dissolved (%).

2.5 Characterization of the solid

X-Ray Diffraction analyses of the synthesized powders were performed using a D8 Bruker Advance diffractometer equipped with a linear Lynx-eye detector using Cu-Kα radiation (λ = 1.5418 Å). The powder patterns were recorded with an angular range from 20° to 120° in 2 theta, with steps of 0.02° and a counting time of 0.5 s per step. The micro-strains and average crystallite sizes were calculated using the Hadler Wagner Langford method as implemented in the JANA 2006 software (Petříček et al., 2014).

The specific surface area of the different oxides was determined with a Micromeritics TriStar II Plus Version 2.02. Nitrogen adsorption was performed at 77 K after an overnight treatment under vacuum at 130°C to ensure their complete outgassing. Such settings and device allow a limit of quantification of 1 m^2 g^{-1} and a statistical error of 5%. For values lower than 5 m^2 g^{-1} the nitrogen is replaced by krypton to minimize the measurement uncertainty to 0.05 m^2 g^{-1}.

The size distribution of the particles is measured before but also after grinding using a Malvern Master Sizer 2000 particle size analyzer. The powders were suspended in a flask and then treated in an ultrasonic bath for 10 min to break the agglomerates. Part of this solution is added to the closed water circuit until the obscurator exceeds a limit value of 13%. The suspension is analyzed three times with an acquisition time of 12 seconds, resulting in a reliable size distribution. For particle sizes smaller than 0.1 µm, dynamic light scattering (DLS) complements laser granulometry. Measurements were performed by the Zetasizer Nano ZS in static mode. A suspension of 1 mL was placed under ultrasound for 5 min and then filtered through a 0.2 µm syringe filter and supplemented with Synthron B03 used as dispersant.

Microstructure analyses of all the powders were also performed using a Scanning Electron Microscope (SEM). The samples were deposited on carbon adhesive tape with additional gold deposit of a few angstroms for CeO_2 treated at 1200°C. A Hitox SH 4000M scanning electron microscope was used to record images with an acceleration voltage of 30 kV under high vacuum conditions.

The nanoscale characterization of milled oxide was carried out with High-Resolution Transmission Electron Microscopy (HR-TEM) after deposition of oxide suspension on carbon coated copper grids. The oxide suspension was previously prepared in water and sonicated in an ultrasonic bath for 8 min. The CeO_2 samples were studied by STEM and EELS by using a Titan Themis (Thermo Fisher) microscope operating at 200 kV.

3. Results

3.1. Oxide characterizations

As already pointed out, two routes were used to synthesize the oxides. The first one, the oxalic precipitation, allow to synthesize ceria powder with typical agglomerated platelets shapes. The SEM observations shown in Figure 1 allow to determine individual platelets median sizes of 15 µm by 8 µm and surface charge effects led to agglomerated pre-sintered particles of a hundred of micrometer width. Several crystallites compose CeO_2 platelets. In literature, some authors referenced that platelet morphology is preserved during calcination, but calcination temperature changes crystallite size. Similar platelet morphologies of CeO_2 particles can be observed from SEM micrographs after 600°C and 1200°C

(Figure 1). The XRD patterns, also in Figure 1, confirm a CeO_2 structure with fluorite-type (PDF card 03-065-2975) for all oxides and highlight the difference of Full-Width Half-Maximum (FWHM) between oxides treated at 1200°C and 600°C. The increase of FWHM at lower calcination temperature gives evidence of a reduction of the crystallite size (i.e. the coherent domain size). In accordance with this,

Table 1 summarizes refinement results of coherent domain size and indicates the increase in size with increasing temperature. The CeO_2 sample treated at 1200°C was afterward defined as the reference of this study, since it possess the largest size, the smallest micro-strain, due to the highest calcination temperature that confer the hardest to dissolve character to this oxide (Claparede et al., 2011a).

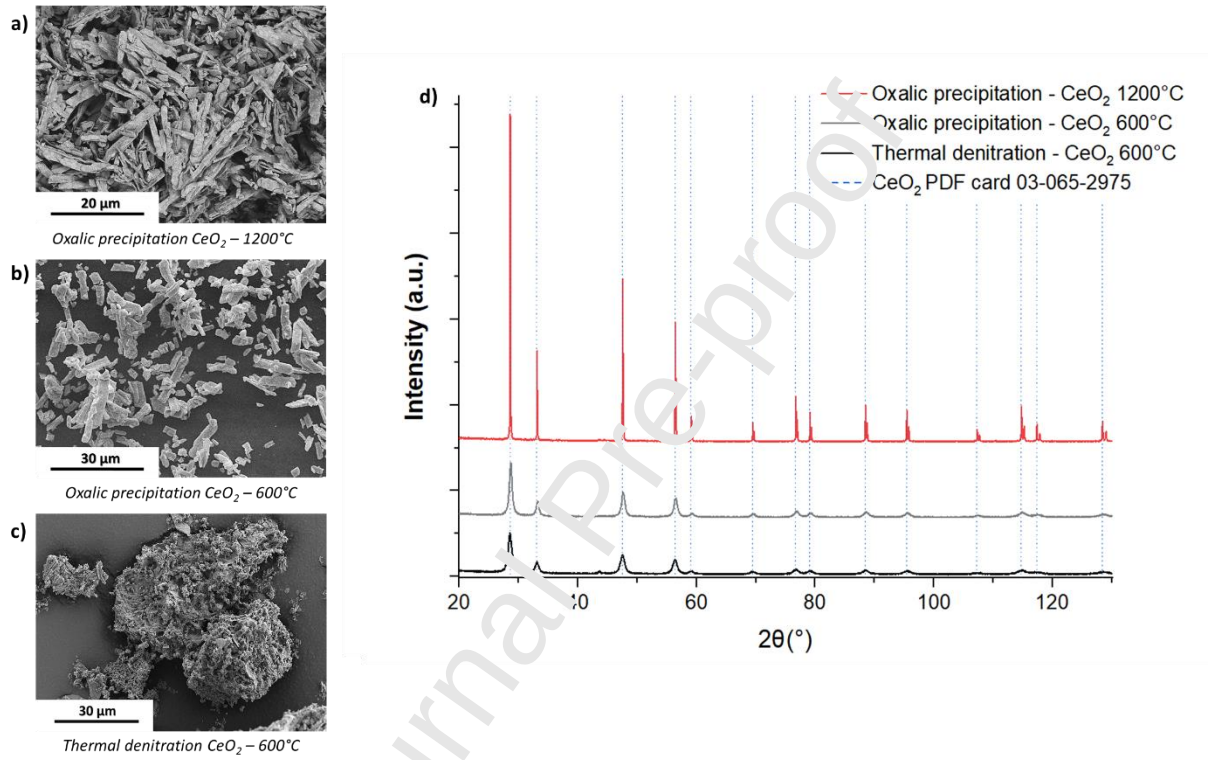

Figure 1 :SEM images of a) cerium oxide obtained by oxalic precipitation and heat treated at 1200°C and b) 600°C for 2 h and c) obtained by second route, advanced thermal denitration and heat treated at 600°C for 2 h. XRD of respective oxides, all corresponded CeO_2 structure (PDF 03-065-2975).

The second route, advanced thermal denitration, allows to synthesize CeO_2 powder batch (Figure 1 d) with a different morphology, i.e. composed of agglomerated nanometric particles. Extracted information from XRD (

Table 1) leads to conclude this oxide batch has a small coherent domain size, equivalent to the oxide obtained by oxalic precipitation and treated at 600°C. Also, these two oxides have similar specific surface area and micro-strain ratio.

Table 1: Specific Surface Area, size of crystallites and micro-strain calculated by Hadler Wagner Langford method from XRD of initial oxides

	SSA (m^2g^{-1})	Size (nm)	Strain (%)
oxalic precipitation - CeO_2 1200°C	0.7	121	$6.5\ 10^{-4}$
oxalic precipitation - CeO_2 600°C	29.8	12	$1.1\ 10^{-2}$

thermal denitration - CeO_2 600°C	30.8	9	$1.4\ 10^{-2}$

3.2. *Study of milled solid*

The oxide sample was ball-milled during 1 h in deionized water at the maximum shaft speed of 4200 revolutions min^{-1} and then, dried during 2 days at 80°C.

The SEM images on particles before and after 1 h milling indicate a change in oxide microstructure (Figure 2). Particles of reference CeO_2 heat-treated at 1200°C before milling correspond to a typical morphology of cerium oxide obtained by oxalic precipitation. The particle milling provokes the formation of porous agglomerates with a bigger specific surface area of 29.8 $m^2\ g^{-1}$ (0.7 $m^2\ g^{-1}$ for raw materials).

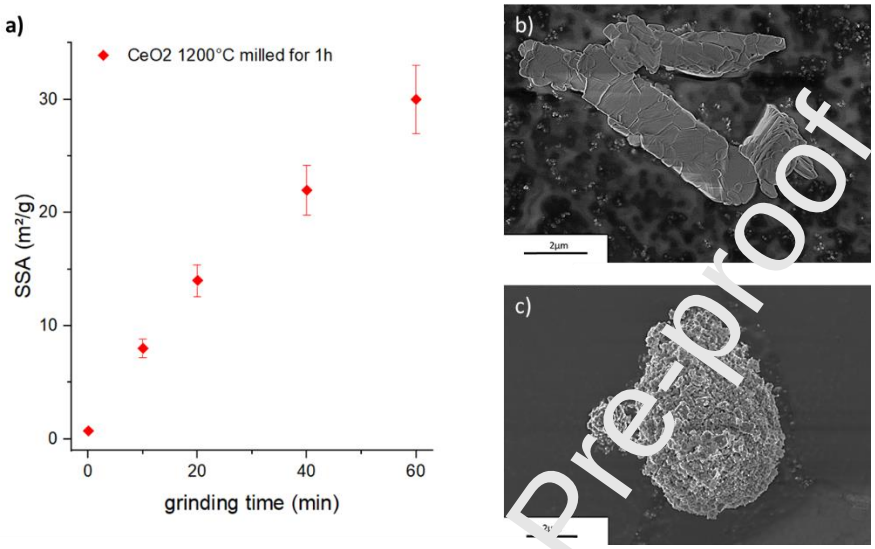

Figure 2 : a) Evolution of specific surface area during grinding CeO_2 heated at 1200°C and SEM image b) before and c) after 60 min of grinding.

The particle size distribution of cerium oxide calcined at 1200 °C is mono-dispersed with an average particle size of 7 µm. The size distribution is between 0.8 and 100 µm. The particle size distribution corresponds to the contribution of the width, length and thickness of the CeO_2 platelets obtained by oxalic precipitation. After one hour of grinding, two distinct populations are visible. The first is made up of nanoparticles with a particle size of 8-10 nm (zetameter) and a second larger in the order of a micrometer (particle size). The use of ultrasound to treat the solution reveals 3 populations on a particle size analyzer: 250 nm / 1-2 µm / 10-20 µm.

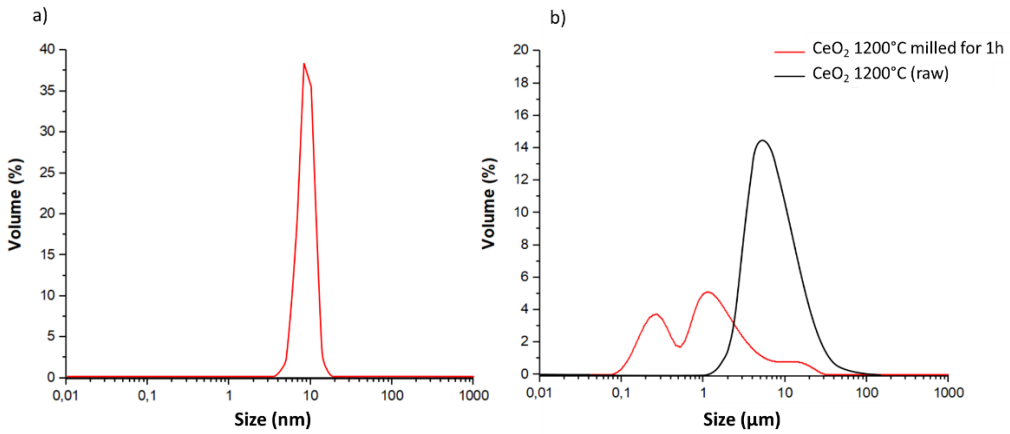

Figure 3 : a) Particle size and b) DLS analysis of CeO_2 before (black) and after grinding (red).

The XRD patterns of CeO_2 powders (reference) are characteristic of a monophasic fluorite-type structure, within Ce^{4+} is surrounded by eight equivalent O^{2-} ions forming the corners of a cube, with each O^{2-} coordinated to four Ce^{4+} ions. The diffractogram of CeO_2 ball-milled during 1 h is also shown in XRD pattern of Figure 4 a). The observed pattern matches to a cubic fluorite-type CeO_2 structure. Upon modification, the peak positions (2θ) of the milled CeO_2 shifted toward a lower angle compared to raw CeO_2. The residual stress in the matrix generates a lattice expansion, leading to a shift in the peak positions. This peak shift to lower angles leads to an increase of cell lattice in agreement with Bragg Law and can be attributed to the formation of Ce^{3+} ions in CeO_2 nanoparticles (Zhang et al., 2002), where the ionic radius increases from 0.970 Å for Ce^{4+} to 1.143 Å for Ce^{3+}. As already reported, the change in oxidative state is accompanied by the loss of O^{2-} (1.380 Å) and creation of oxygen vacancies (1.164 Å), affecting also the volume of CeO_{2-x} (Lee et al., 2011; Spanier et al., 2001). In addition, as expected, milled oxide's diffraction pattern present higher Full-Width Half-Maximum (FWHM) than un-milled reference oxide, which involve the reduction of crystallite size in agreement with images (Deshpande et al., 2005).

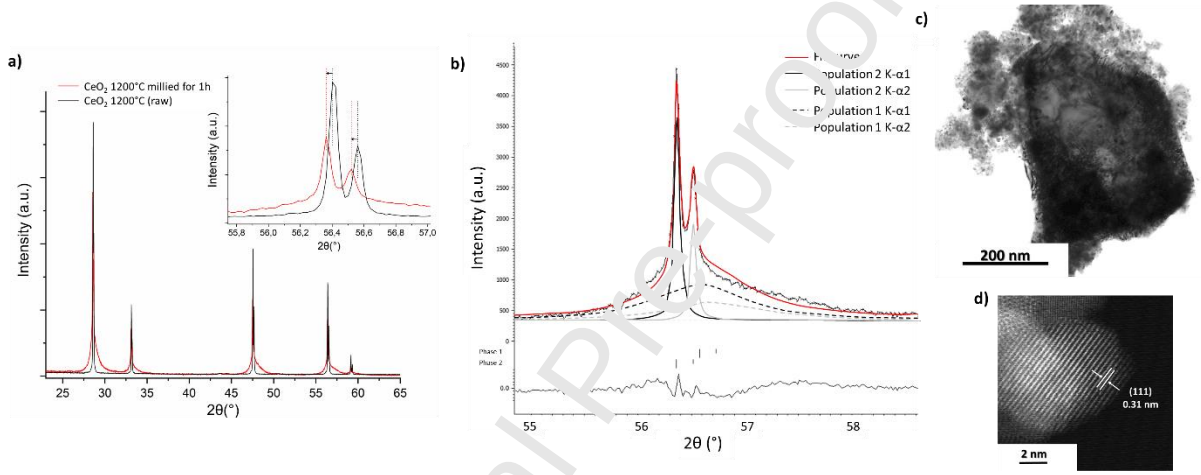

Figure 4 : a) XRD patterns of the CeO_2 before (red) and after (black) 1 hour of ball-milling. The inset displays the shifting and broadening of the peaks b)TEM images of CeO_2 before grinding with nanoparticles and grain and c) High-resolution scanning TEM images of nanoparticles showing sets of <111> planes and surfaces d)TEM-HR image of a nanoparticle.

Table 2 : Specific Surface Area, size of crystallites, strain and lattice parameter calculated by Fundamental parameters approach from XRD of initial oxides milled during 1 h.

CeO_2 1200°C milled for 1 h	SSA (m^2g^{-1})	Size (nm)	Strain (%)	Lattice parameter (Å)
Population 1	29.5	9	$4.0\ 10^{-2}$	5.3741
Population 2		150	$2.1\ 10^{-3}$	5.4101

The (S)TEM images (Figure 4 c) and d)) and fitting of XRD peaks (Figure 4 b and interpretation in Table 2) reported the presence of a bimodal population after one hour of grinding, nanoparticles (Figure 4 c) and particles with size similar to that of initial crystallite before grinding. In accordance with this result, peaks deconvolution find the presence of two populations, nanoparticles and micronic particles with a higher micro-strain ratio than that before grinding. A deeper study of these coarse grains revealed the presence of some defects (see after TEM study). The diffraction peak fits show the presence of four curves, i.e $K_{\alpha1}$ and $K_{\alpha2}$ from two populations. The first, whose contribution is in full line, corresponds to population 2, the large grains. The second contribution, in dotted line, is attributed to population 1, nanosized ones. Table 1 allows to identify the information processed by these fits. Lattice parameter of population 2, particles with similar size to that of initial crystallite before grinding, correspond to a typical CeO_2 (5,4101 Å), but

population 1, nanoparticles has a smaller parameter (5.3741 Å). Previous results from literature (Hailstone et al., 2009; Younis et al., 2016; Zhang et al., 2004a) had demonstrated that the lattice parameter progressively decreases due to the inclusion of Ce^{3+} ions with a smaller ionic radius. Some authors had explained this shoulder at wide angles by the formation of nanohybrid (Ma et al., 2016) composed by Ce_2O_3/CeO_2. The CeO_2/Ce_2O_3 nanocomposite exhibited a similar diffraction pattern, but with the maxima shifted towards higher diffraction angles. It is clear that nanocomposites exhibited a greater number of Ce^{3+} ions, indicating a highly reducible nature of the nanostructures.

3.2.1. Defects on grain

These defects corresponding at a dislocation area, as indicated by the appearance and disappearance of a line contrast at a specific orientation. The steps observed in Figure 5a (dark part on the left, the light area represents the void) reveal the sliding of the crystalline planes relative to each other. These types of atomic steps can only be observed in areas of shear that are finished as a free surface (as observed on Figure 5) or at grain joints. They are the manifestation of the movement under the effect of the mechanical forces, of linear defects present in the crystal. The diffraction plane treatment by FFT shows the effect of introduction of an atomic half-plane inside the atomic planes at several places circled in red in Figure 5. Concentration of multiple dislocations can be identified on this strain zone. Dislocations, corresponding to the black lines present in the grains, are also observed on a larger scale. This contrast results from the decrease in the intensity of the transmitted beam linked to network distortions that locally modify the deviations from the Bragg angle near a defect. Two kinds of dislocation were identified, one extends through grain (Figure 5b) and the other (larger and shorter) accumulate at the point of initiation of the ball impact and abrade the surface (Figure 5c)

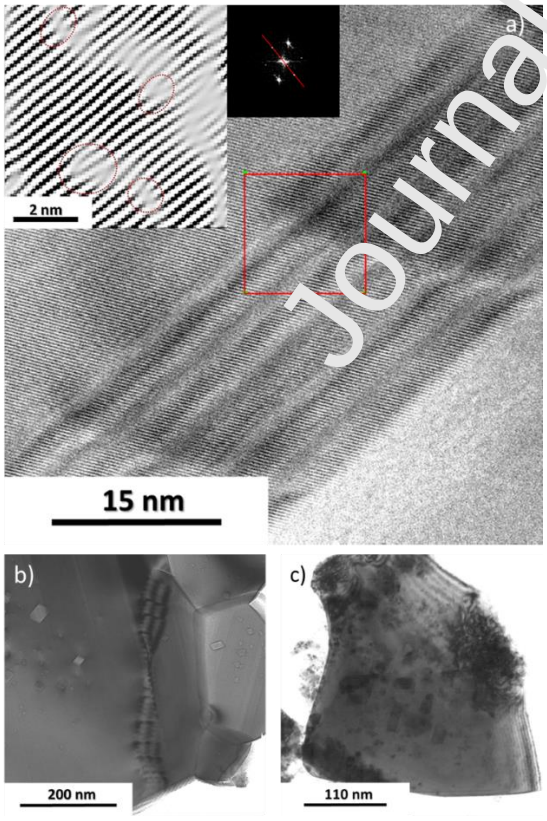

Figure 5 : a) A high-resolution TEM image of steps in massive grain surface of the ball-milled CeO_2 sample and by FFT highlights the presence of dislocations b) linear dislocation through the grain and strain field around c) accumulation of black arc reflecting the presence of dislocations.

3.2.2. CeO_2 NPs

Oxidation state of Ce in two nanoparticles of 7.8 nm and 4.3 nm, indicated by orange circles in HAADF-STEM image in Figure 6 a) were analyzed using EELS spectroscopy. Figure 6 b) demonstrates a local oxidation state map of Ce^{3+} (red) and Ce^{4+} (yellow). Local EELS spectrum corresponding area 1 to 4 are shown in Figure 5 c). The $M_{4,5}$ edges on spectra are characteristic of transitions of 3d core electrons to unoccupied states of p- and f-like symmetry. The sharp M_5 and M_4 peaks (Figure 6 c)) arise from transitions from initial $3d^{10}4f^n$ state to the final $3d^94f^{n+1}$ state. The Ce^{4+} M_5 and M_4 edges (Figure 6 c)1) are separated by 18.1 eV and are composed of two main symmetrical maxima at 887.7 and 905.8 eV, and two broader and shorter maxima at 892.7 and 910.2 eV. The main M_5 and M_4 maxima of CeO_2 result from transitions from an atomic-like f^0 ground-state configuration. The Ce^{3+} $M_{4,5}$ edge shapes, intensities, and energies differ from those of Ce^{4+}. The Ce^{3+} (Figure 6 c)) M_5 edge displays a weak peak at 885.5 eV while the M_4 edge is more asymmetrical with a feature at 903.3 eV. In zone 1, corresponding to the core of the particle, the spectra have a typical form of Ce^{4+}. However, at the particle surface (zone 3) the spectrum revealed Ce^{3+} feature. In the case of the nanoparticles, the Ce^{3+}/Ce^{4+} concentration decreases with the increase of particle size, as previously observed on similar samples, consistently with the reduced shell formation around an oxidized core (Spadaro et al., 2016, Turner et al., 2011). In the small particle (4.6 nm in diameter indicated as zone 4), Ce^{4+} ions were totally reduced into Ce^{3+}. It is immediately apparent that the surface reduction shell is present over the whole particle surface. At its thinnest, the Ce^{3+} shell appears to extend over approximately 2 nm.

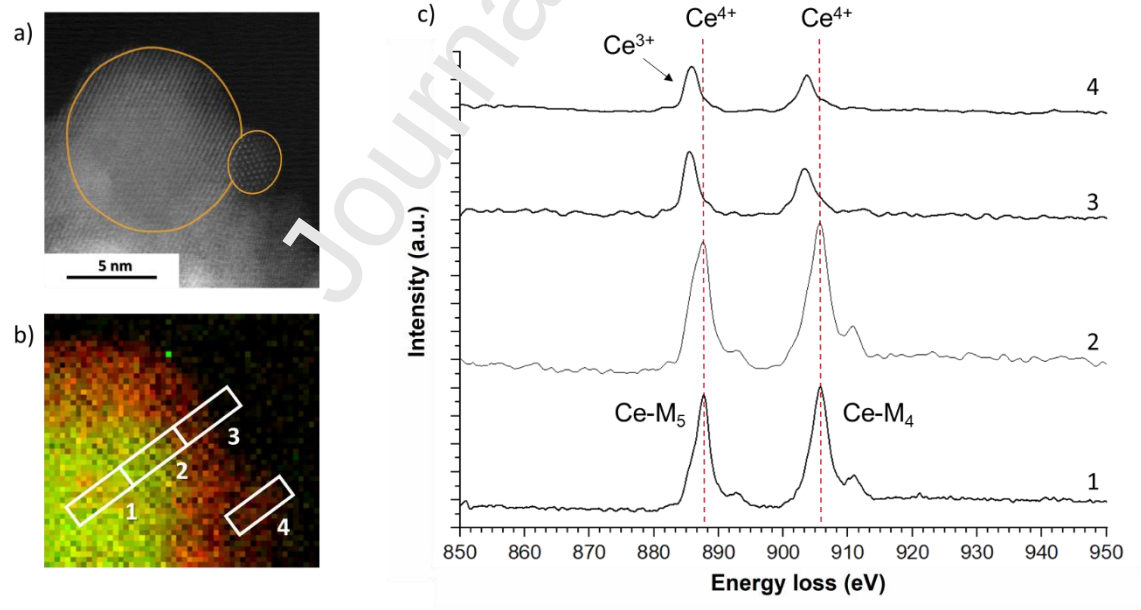

Figure 6 : a) STEM-HR of CeO_2 NPs after one hour of ball-milling b) EELS maps of Ce^{3+} (red) and Ce^{4+} (green) oxidation state distribution c) Averaged Ce $M_{4,5}$ spectra from regions 1,2, 3 and 4 on the NPs EELS map.

The mechanism of such reduction due to particle size reduction is well explained in “Cerium Oxide Nanostructures and their Applications” | IntechOpen, 2019. Increase in surface area per volume ratio leads to electronic changes ending to oxygen non stoichiometry $CeO_{2-\delta}$. Each free oxygen atom creates oxygen vacancy that reduces two cerium (Ce $4f^0$) on cerium (Ce $4f^1$) by electron transfer. Thus, a neutral

species ½O_2 (g) is formed if an oxygen ion (O^{2-}) leaves the ceria lattice. The two electrons left behind are trapped at two cerium sites, i.e. they become localized at two cerium sites. At such cerium sites, the electron prefers to occupy an empty Ce4f state that splits the Ce4f band into two sub-bands: an occupied Ce4f full band and an empty Ce4f band. In CeO_2 bulk material an empty narrow 4f band is located between conventional valence bands (O2p and Ce5d). As progressive reduction of the oxide occurs it first concerns less coordinated atoms that exhibit weaker electrostatic potential. Practically, the reduction limit of non-stoichiometric ceria is Ce_2O_3, where all cerium ions are found in a Ce^{3+} oxidation state. The electronic band structure of Ce_2O_3 bears resemblance to that of partially reduced ceria, in which Ce4f empty and Ce5d bands have been merged together in the conduction band.

3.3. Dissolution

3.3.1. Dissolution before/after milling

In order to compare the influence of milling, dissolution tests of CeO_2 calcined at 1200°C were carried out in 8.5 M nitric acid at 95°C. It corresponds to the black curve in Figure 7. After 6 hours, the final dissolution efficiency is 0.1% of the initial oxide amount. Oxides calcined at high temperature has a strong refractory character to dissolution, in agreement with a low final dissolution efficiency and other information in the literature (Claparede et al., 2011b). Kinetic plot is linear, contrary to CeO_2 reference ball-milled during 1 hour (Figure 7). This same oxide calcined at 1200°C was ball-milled before being dissolved in the same conditions. The kinetics can be split into two regimes, the first one extends up to 30 min; at the end of this first step, dissolution rate was close to 20%. During the second step, it grows up to 36% after 6 hours. Kinetics of the first regime is fast; even if the second regime is slower than the first one, it is faster than the dissolution of the non-activated oxide. The effect of grinding on the CeO_2 dissolution is significant, as the dissolution rate increases by a factor of 360.

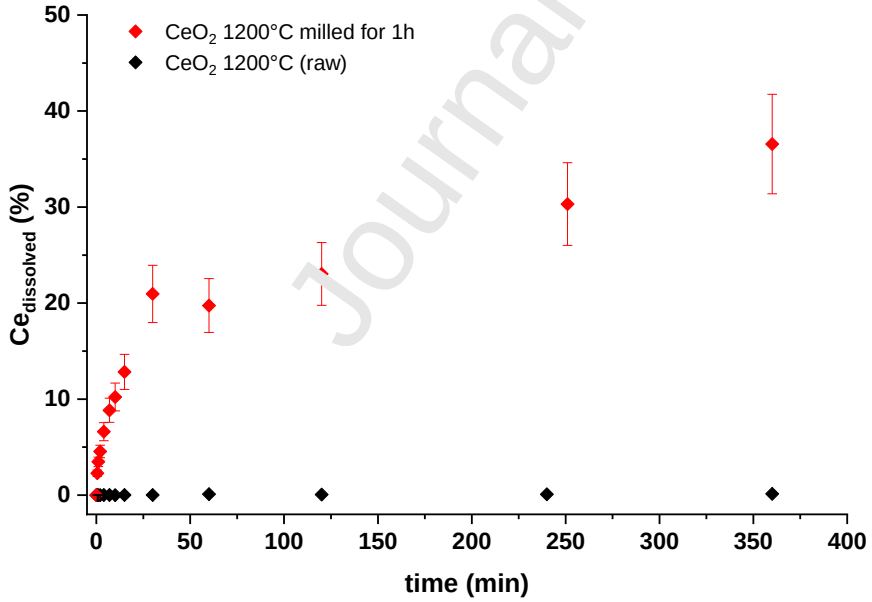

Figure 7 : Comparison between dissolution kinetics of CeO_2 calcined at 1200°C un-milled (black) and ball-milled CeO_2 (red) in nitric acid 8.5 M, 90°C with an initial solid/liquid ratio of 300 mg / 15 mL, stirring rate of 400 revolutions min^{-1}

3.3.2. Kinetic dissolution comparison with similar characteristics materials

The ball-milled ceria dissolution (red curve) was compared to two other materials prepared at lower temperature. Figure 8a shows the comparison of dissolution kinetics of ball-milled product of CeO_2 calcined at 1200°C (the previous one) with the dissolution kinetics of un-milled CeO_2 obtained via the same oxalic route but calcined at 600°C. Both oxides exhibited similar specific surface area (29.5 $m^2\ g^{-1}$ vs 29.8 $m^2\ g^{-1}$). However, the un-milled oxide presents a final dissolution efficiency of only 13% and an almost linear kinetic plot unlike the ground sample. To illustrate if this kinetics difference is due to different morphologies (nanoparticle agglomerates vs rod massive grains), dissolution kinetics for ball-milled CeO_2 at 1200°C and NPG CeO_2 have to be compared (Figure 8b). It shows that both samples exhibit the same specific surface area and also a morphology composed of nanoparticle agglomerates (Figure 1). Once again, dissolution of the un-milled sample only reaches 13% compared to the ball-milled sample (36%) with an almost linear kinetics.

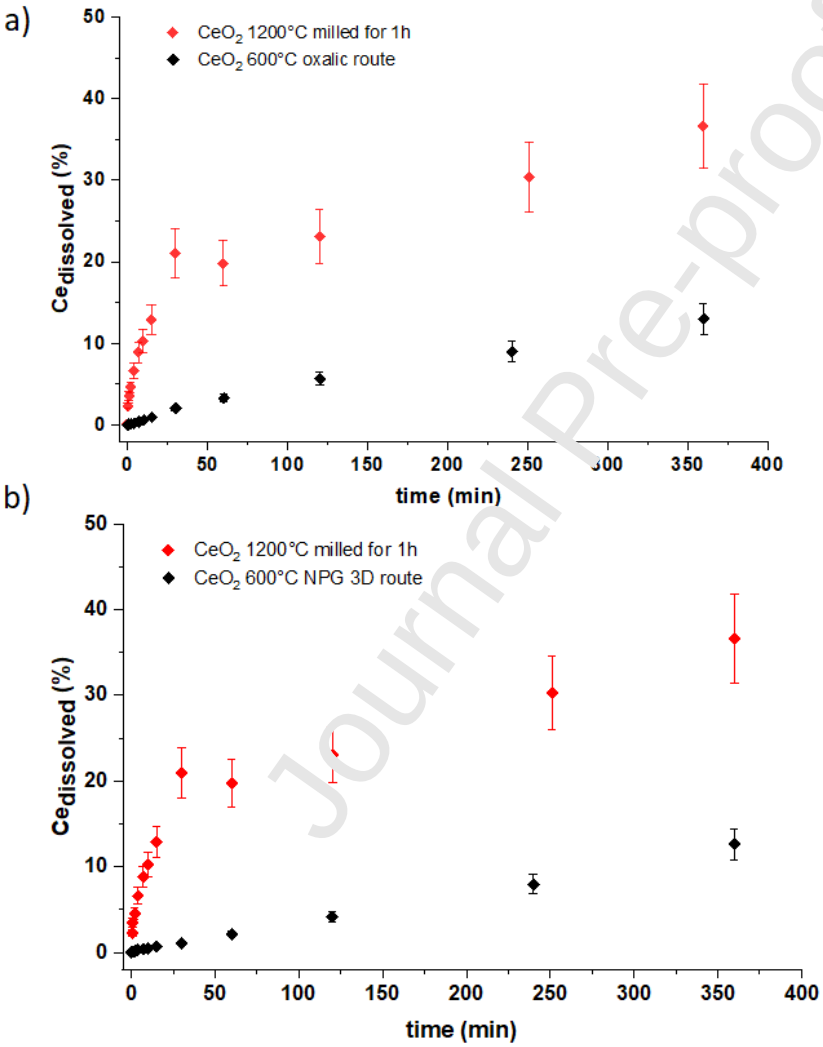

Figure 8 : Comparison between dissolution kinetics of CeO_2 calcined at 1200°C milled CeO_2 (red) and a) CeO_2 with same SSA and obtained via oxalic precipitation and treated at 600°C (black) and b) CeO_2 with same SSA and same morphology, obtained via NPG route and fired at 600°C (black) in nitric acid 8.5 M, 90°C with an initial solid/liquid ratio of 300 mg / 15 mL, stirring rate of 400 revolutions min^{-1}.

4. Discussion

4.1. Fragmentation mechanism

Particle size and DLS analyzes (Figure 3) indicate that the category between 10 and 20 µm corresponding to chipped platelets does not represent a significant part by volume (a small percentage <10%) and is therefore not very abundant. The second population, a few micrometers long, is more predominant and corresponds to detached or broken platelet grains. Finally, the last population consists of the largest nanoparticles.

The observation of the evolution of particle size during milling by Scanning Electron Microscope (Figure 9 a,c,e) allows to propose a fragmentation mechanism. Statistical analyses of recorded images confirm the progressive decrease in particle size related to grinding. First, these images show a rupture of the platelets characteristic of oxides obtained by oxalic precipitation. Each platelet is itself made up of crystallites with variable sizes. When these platelets fragment, grain boundary density decreases until fragments of equivalent size are obtained. After one hour of grinding, fragments have become, for the great majority, crystallites (that initially composed these fragments). Data acquisitions by TEM (Figure 8 b,d,f) confirm the presence of two mechanisms. For grinding times less than 40 min, holes with grain shape are observed, evidencing of the pullout of former grains. Beyond these 40 min, the majority of the grains have reduced in size. Comminuted solid consists of a few crystallites (platelet residue) with contrast black lines, attributed to dislocations.

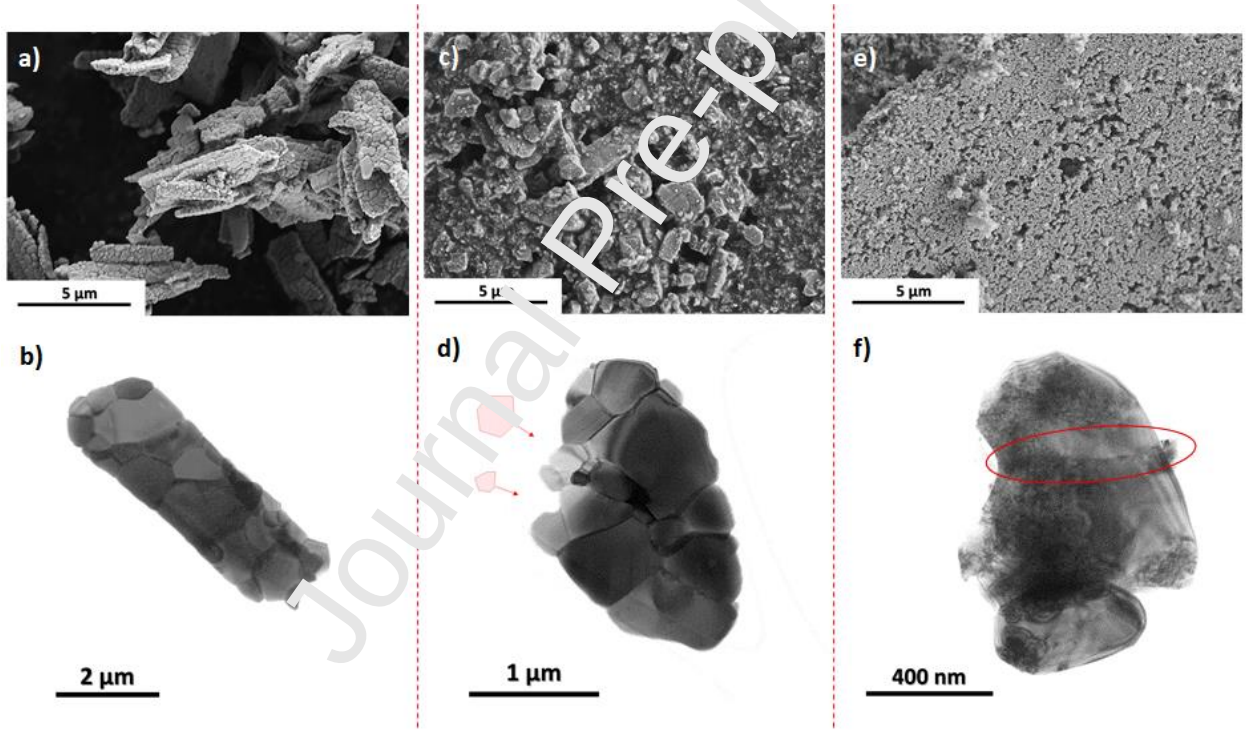

Figure 9 : Evolution of microstructure during milling at 0 min a) and b), 20 min c) and d) and 60 min d) and e) by SEM and STEM respectively.

4.2. Contribution of milling on dissolution

The comparison of the dissolution kinetics between raw and ground CeO_2 shows an increase in the dissolution rate by a factor of 360. The non-activated oxide has a 0.1% dissolution rate after 6 h in HNO_3 95 °C while the activated solid has been dissolved to an extend of 36%. The dissolution kinetics of milled oxide, can be described like a kinetics in two different stages, unlike raw oxide. The first one is fast while the second one is slower as described on Table 3. The activated oxide kinetics, even for the slowest stage, is faster than the kinetics of the raw oxide.

Table 3 : Slope equation of CeO_2 calcined at 1200°C un-milled and ball-milled CeO_2 (two stages)

		Slope equation (% min^{-1})
CeO_2 1200°C (raw)		$\%Ce_{dissolved} = 3.74\ 10^{-4}\ t + 5.79\ 10^{-3}$
CeO_2 1200°C milled for 1 h	t < 30 min	$\%Ce_{dissolved} = 6.42\ 10^{-1}\ t + 2.80$
	t < 30 min	$\%Ce_{dissolved} = 5.60\ 10^{-2}\ t + 1.639\ 10^{1}$

Normalization to same SSA is not sufficient to explain this difference in kinetics as SSA grows only by a factor of 42, meaning dissolution kinetics acceleration cannot be only due to increase in specific surface area induced by size reduction. When the particle sizes decrease the dissolution kinetic increase (Claparede et al., 2011b). Not everything can be explained on the basis of size reduction, but this was the main factor. The particle size decreased and the specific surface area increased to a final value of 29.8 m²/g after grinding for 1 h.

Then, dissolution of the milled cerium oxide is compared to the dissolution of a cerium oxide also obtained by oxalic precipitation but calcined at a lower temperature in order to obtain equivalent specific surface area (29.8 m²/g) and coherent domain size (~12 nm). Despite these similar parameters for these two samples, dissolution kinetics of the un-milled oxide only reached 12% compared to the 36% observed on ball-milled oxide. However, despite both oxides were made using the same synthesis route, morphology of both samples is different due to the milling (Figure 2). The ball-milled oxide exhibits a microstructure made of nanoparticle's agglomerates and grains resulting from decohesion (Figure 4), while the 600°C annealed-raw oxide is made of aggregated platelets of about 20 µm size. One could, at first sight, assume that dissolution kinetics differences could result from such morphological changes.

To overcome the contribution of morphology, the dissolution of milled cerium oxide was compared to the one of a cerium oxide obtained by NPG route and calcined at 600°C. Both oxides have similar specific surface area (30.8 m²/g), similar crystallite sizes (~10 nm) and a comparable morphology (agglomerated nanoparticles). The dissolution kinetics are still different, the final dissolution efficiency achieved was only 14% for NPG route, compared to 36% for the ball-milled sample. Therefore, grinding makes an additional contribution different from reduction of particle size and change in morphology. On top of the increase in terms of dissolution efficiency (%), dissolution kinetics of the ball-milled sample shows two regimes and not only one as observed on the two other samples.

The cerium oxide dissolution is thermodynamically impossible by the acid itself (ΔG_0=40 kJ mol^{-1} (Beaudoux et al., 2016)). It is only possible thanks to the complexation with the nitrate ions following the chemical reaction $(CeO_2)_{solid} + 4\ HNO_3 \rightarrow Ce(NO_3)_{4\ aq} + 2\ H_2O$. According to the transition state theory and the collision theory to promote dissolution, it is necessary to provide sufficient energy called the activation energy, to reach the transition state. This transition state corresponds to the activated complex, as shown Figure 10 (red line) that depicts a situation for dissolution of an unmilled ceria where the molar free energy of the dissolved and totally solvated species at the solvation plane is lower than in the oxide surface. As a dissolving species moves across the double layer there is an initial increase in chemical free energy, to reach a peak as it becomes a partially solvated activated complex, then decreasing as it approaches and becomes totally solvated at the solvation plane. The activation energy for dissolution is noted $\overrightarrow{\Delta G_{CeO2}}$ and the Ce^{4+} solution passage is $\overleftarrow{\Delta G_{Ce^{4+}}}$, where $\overrightarrow{\Delta G_{CeO2}} < \overleftarrow{\Delta G_{Ce^{4+}}}$.

To promote the dissolution beyond the surface effect, it is necessary to minimize the activation energy to reach the activated complex. In the case of ceria, the size reduction is accompanied by an oxidation state change. Analysis of the milled solid by XRD, STEM and EELS showed the presence of two populations.

The nanoparticles exhibited a shell-core effect for diameter greater than 5 nm, below this limit particle was completely reduced. The shell has a thickness of approximatively 2 nm and is composed of Ce^{3+}. Some authors had exploited this phenomenon, Ce^{3+} confers to the material some properties as ability to store and transport oxygen in catalysis. Corkhill et al. (2016) demonstrated that sub stoichiometry of cerium oxide has a greater effect than the contribution of particle size on dissolution kinetics ($\overleftarrow{\Delta G}_{Ce^{3+}} < \overleftarrow{\Delta G}_{Ce^{4+}}$) (Zhang et al., 2004b). By a charge compensation for oxygen vacancies, ionic radius between Ce^{3+} and Ce^{4+} decreases that contracts the fluorite cell. This contraction exhibits significant internal lattice strain, $\overrightarrow{\Delta G}_s$ that reduces the activation energy $\overrightarrow{\Delta G}_{CeO_{2-x}}$ (lower than $\overrightarrow{\Delta G}_{CeO2}$) in favor for the dissolution (green line Figure 10).

The activation energy can also be reduced by increasing the Gibbs free energy in the material surface. As observed, grinding has generated defects such as dislocation that change locally the plasticity on particle. Several studies (Albanese-Kotar and Mikkola, 1987; Benzerga et al., 2005; Blum et al., 1990) have already shown that when the concentration of dislocations increases, the dissolution is better. They have been modelized through equation 3 (Tromans and Meech, 2001), where :

$$\Delta G_d \approx (\rho_d M)\frac{b^2\mu}{4\pi}\ln\left(\frac{2(\rho_d)^{-1/2}}{b}\right) \quad \text{(Equation 3)}$$

ρ_d : the dislocation density
M : the molar volume of the mineral
μ : the elastic shear modulus
b : the Burgers vector

The stored energy, $\overrightarrow{\Delta G}_d$ decreases the activation energy $\overrightarrow{\Delta G}_{CeO_{2+\varepsilon}}$ (red dotted line in Figure 10) compare to the activation energy of the unground oxide $\overrightarrow{\Delta G}_{CeO2}$ and also promotes the dissolution rate. Dislocations provide favorable reactive sites, by their presence on the surface and the creation of steps, for localized chemical attack. Other materials have shown higher dissolution rates with increasing density of dislocation.

In the present case, defects such as dislocations, strain and oxygen vacancies (Ce^{3+}) provoke the increase of initial activation energies in the solid. The activation energy required to reach the state of the activated complex is then lower than in the case of dissolution of non-activated CeO_2. All these contributions can be responsible for the increase of dissolution rate.

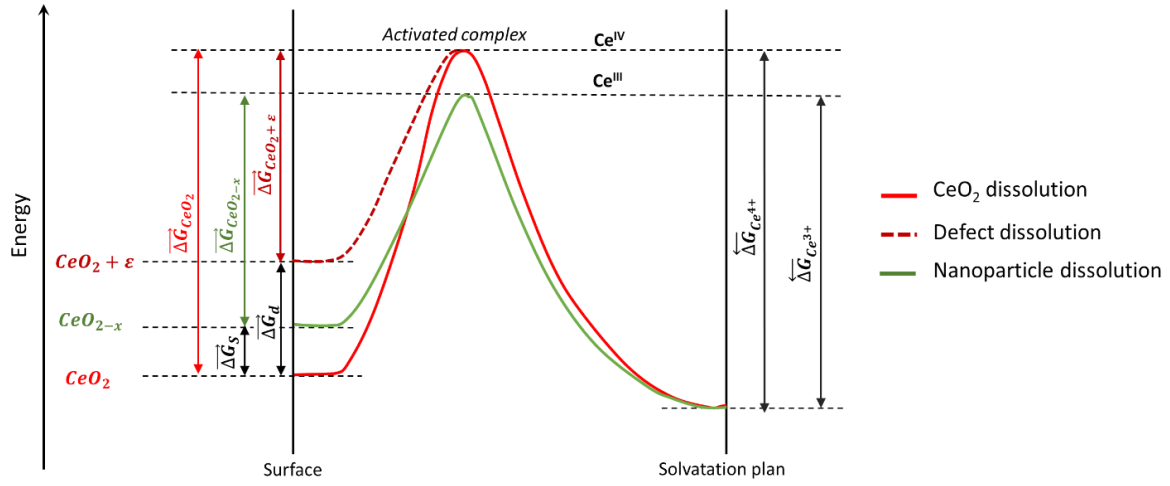

Figure 10 : Schematic diagram of the energy landscape of the solid after grinding. Three ways, in red the classic dissolution of CeO_2, in green the dissolution of CeO_2 containing Ce^{3+} and in red dotted line, the dissolution path of CeO_2 containing defects.

4.3 Phenomenon identification

Figure 11 shows the comparison of dissolution kinetics of CeO_2 milled for 1 h, CeO_2 calcined at 1200°C (raw) and CeO_2 calcined at 600°C (from oxalic precipitation) with the model from Ziouane *et al.*(2018) given by Equation 1. Note that this model was established from dissolution kinetics of oxides which have not been modified by any process such as grinding meaning it was built on ceria with no partial reduction. When the model is applied to cerium oxide obtained by oxalic precipitation and calcined at 600°C, the kinetics of dissolution measured correspond to the model ($3.36\ 10^{-2}$ % dissolved min^{-1} vs $3.64.10^{-2}$ % dissolved min^{-1} Table 4). Similarly, when applied to the reference material before milling (1200°C raw) (Tc = 120 nm and SBET = 0.7 m^2g^{-1}) slope of experimental fit is of the same order of magnitude as the modelled figure (less than a factor 3 of difference that is on the model error bar: $3.74.10^{-4}$ % dissolved min^{-1} vs $9.75.10^{-4}$ % dissolved min^{-1}Table 4). Therefore, when applied to unground ceria Ziouane *et al.*'s model returns a good prediction.

At first sight, this model does not explain the dissolution of the ground material, as it does not predict the splits into two distinct regimes. In addition, the first regime, faster, does not correspond to any slopes of the model applied to the crystallite sizes determined by refinement of the X-ray diffractogram and specific surface area of the ground powder (Table 4). Reversely, for the model to match with dissolution fit of this first regime, the coherent domain size would have to be about 0.61 nm, which does not make physical sense. Therefore, dissolution of CeO_2 at exact oxygen stoichiometry cannot be the phenomenon controlling this regime and combination of size reduction and Ce(+III) dissolution is more likely responsible to this faster dissolution regime.

The second regime is of the same order as that simulated from particles composed of crystallites of 7 nm long. This slope is also similar to the dissolution of CeO_2 obtained by oxalic precipitation and calcined at 600°C ($5.60.10^{-2}$ % dissolved min^{-1} vs $3.64.10^{-2}$ % dissolved min^{-1} Table 4).

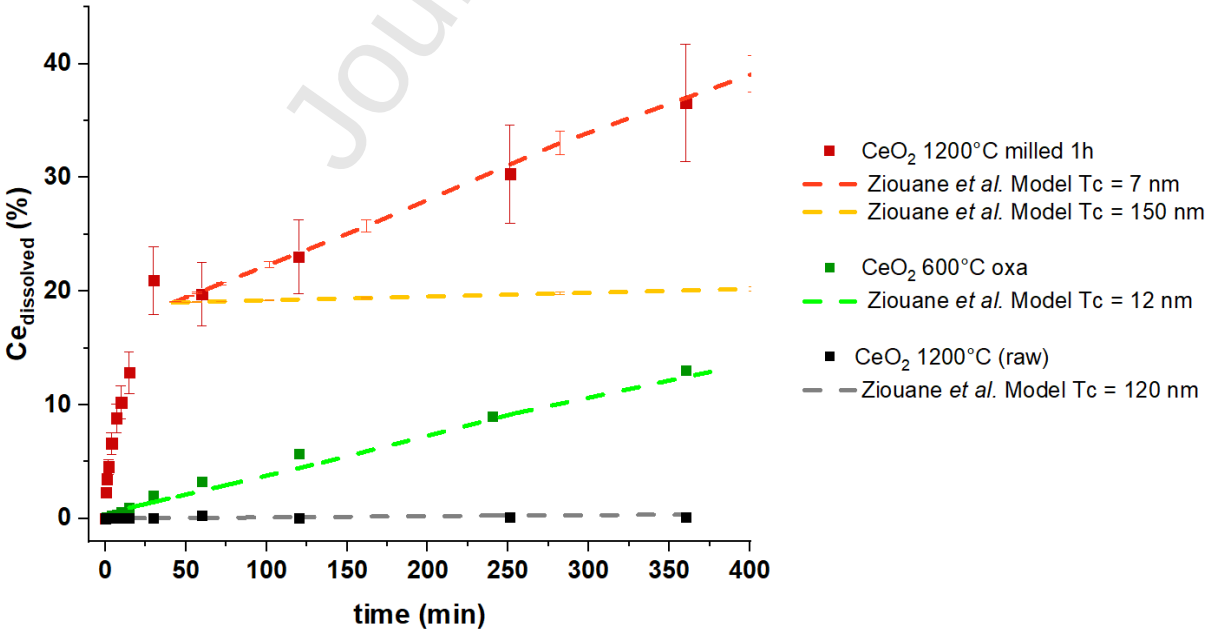

Figure 11 : dissolution kinetics of the reference oxide before (black dots) and after millng (red dots) compared to dissolution kinetics of CeO_2 600°C oxa (green dots) and kinetics modeled by Ziouane et al. (2018) from crystallites

(red curve) of 7 nm, of (orange curve) 150 nm, of (grey curve) 120 nm and of 12 nm (green curve) by XRD refinements.

Table 4: Fit equations of dissolution experimental kinetics (grey lines) of the reference oxide before and after milling,

	Tc (nm)	**SSA (m^2g^{-1})**		**Slope equation (% min^{-1})**	**R^2**
CeO_2 1200°C milled for 1 h	9	29.5	t < 30 min	$\%Ce_{dissolved} = 6.42\ 10^{-1}\ t + 2.80$	0.954
	150		t < 30 min	$\%Ce_{dissolved} = 5.60\ 10^{-2}\ t + 1.639\ 10^{1}$	0.999
Ziouane et al. (2018) model Tc = 7 nm	7	29.5		$\%Ce_{dissolved} = 5.60\ 10^{-2}\ t$	1
Ziouane et al. (2018) model Tc = 150 nm	150	29.5		$\%Ce_{dissolved} = 2.68\ 10^{-3}\ t$	1
CeO_2 600°C oxa	12	29.8		$\%Ce_{dissolved} = 3.64\ 10^{-2}\ t + 3{,}43\ 10^{-1}$	0.987
Ziouane et al. (2018) model Tc = 12 nm	12	29.8		$\%Ce_{dissolved} = 3.36\ 10^{-2}\ t$	1
CeO_2 1200°C (raw)	120	0.7		$\%Ce_{dissolved} = 3.74\ 10^{-4}\ t + 5.79\ 10^{-3}$	0.995
Ziouane et al. (2018) model Tc = 120 nm	120	0.7		$\%Ce_{dissolved} = 9.75\ 10^{-4}\ t$	1

of the calcined oxide at 600°C and comparison with model with similar crystallite sizes and specific surface area.

For CeO_2 600°C oxa, the particles with a platelet form have an actual size within the order of a micrometer but with a size of the coherent domains of 12 nm. The second regime of dissolution of the milled oxide is very close to the dissolution of such type of sample (platelet residues not having reached the nanometric scale but whose crystallites have been reduced to around 10 nm). However, the milled solid consists of two populations composed of partially or totally reduced nanoparticles and residues of micron platelets with average crystallites size of 150 nm. If the coherent domains of the particles of the reference oxide milled for 1 h are 150 nm, i.e. the same size as those of the unground sample (gray curve Figure 11), the dissolution kinetics should have been equivalent and therefore very low (orange right Figure 11). However, as Table 4 shows, these kinetics are not in the same order of magnitude.

To explain the match of the kinetics of the second regime with dissolution of a material with smaller coherent domains, the solid have to correspond to grains containing dislocations. As illustrated in figure 5b, the ground particle exhibits such smaller crystallites. The one shown in Figure 5b is divided into two by a dislocation and form two distinct smaller coherent domains.

5. Conclusion

Grinding has made possible an increase in dissolution kinetics of cerium oxide known to have a refractory character for dissolution. The significant improvement of dissolution rate results in an increase by a factor of 360 over an unground oxide. The dissolution of different powder batches having similar specific surface area and morphology have shown that the effect of grinding on the dissolution was not only explained by the sole effect of size reduction. Analyses of the solids showed that the grinding resulted in structural and microstructural modifications. After one hour of grinding, the solid presents two populations. A first one made of nanoparticles exhibiting the surface reduction. The second population corresponds to grains resulting from the milled platelets containing a lot of internal stress (contrast on the STEM images) and dislocations crossing or accumulating in the grains. The reduction of particle size promotes a formation of Ce^{3+} layer at the surface of nanometric particles which improves dissolution efficiency. A second

explanation to understand the increase in kinetics of dissolution would be linked to the creation of steps on surface and defects in the solid including the dislocations. These dislocations generate plastic deformations that are irreversible in CeO_2. It also increases the internal energy inside the material. During dissolution, this released energy enhances dissolution kinetics by diminishing the activation energy to facilitate dissolution.

The present work revealed three important phenomena in the CeO_2 dissolution; the reduction in size linked to the dissolution of particles, the dissolution of Ce^{3+} and the relaxation of dislocation and internal energy. Ziouane *et al.*'s model analysis made it possible by analogy to identify that the second regime is governed by the dissolution of particles containing dislocations reducing the size of coherent domains. The mechanism behind the first kinetic dissolution regime seems to be linked to the dissolution of partially reduced nanoparticles.

Ceria and plutonium oxide both being ceramics and exhibiting the same behavior at failure and ceria being also often used as PuO_2 safe analogue for dissolution studies, this dissolution process could be applied to plutonium oxide materials. Therefore, high energy milling on PuO_2 would produce nanoparticles too. Moreover, despite no size effect has been observed yet in the literature for plutonium oxide, Pu (+III) does exist and it is well known that reductive dissolution of PuO_2 is faster than dissolution with no oxidation state evolution (Machuron-Mandard et al.,1989; Beaudoux et al., 2016b), like oxidative dissolution ending with PuO_2^{2+} (Bourges et al., 1986). Reductive dissolution is not in use at industrial scale because it is difficult to maintain reductive conditions in nitric acid, medium for liquid/liquid partitioning following dissolution step in used fuel recycling treatment. If reduction occurs via mechanical activation as for ceria this would not be a problem. The Pu^{3+} would simply be better oxidized naturally by nitrous acid present in the dissolution liquor.

6. Acknowlegment

Financial support for this research was provided by the European Commission (project: GENIORS - GEN IV Integrated Oxide fuels Recycling Strategies (grant number 755171))

Declaration of interests

The authors declare that they have no known competing financial interests or personal relationships that could have appeared to influence the work reported in this paper.

The authors declare the following financial interests/personal relationships which may be considered as potential competing interests

References

Agarwala, K.P., Naik, M.C., 1961. Kinetics of decomposition of yttrium, cerous and zirconyl oxalates. Anal. Chim. Acta 24, 128–133. https://doi.org/10.1016/0003-2670(61)80027-5

Albanese-Kotar, N.F., Mikkola, D.E., 1987. Dissolution of comminuted magnesium oxide as affected by the density of dislocations introduced by various comminution methods. Mater. Sci. Eng. 91, 233–240. https://doi.org/10.1016/0025-5416(87)90302-8

Baláž, P., Ficeriová, J., Šepelák, V., Kammel, R., 1996. Thiourea leaching of silver from mechanically activated tetrahedrite. Hydrometallurgy 43, 367–377. https://doi.org/10.1016/0304-386X(96)00015-1

Beaudoux, X., Virot, M., Chave, T., Durand, G., Leturcq, G., Nikitenko, S.I., 2016a. Vitamin C boosts ceria-based catalyst recycling. Green Chem. 18, 3656–3668. https://doi.org/10.1039/C6GC00434B

Beaudoux, X., Virot, M., Chave, T., G., Leturcq, G., Jouan G., Venault L., Moisy P. and Nikitenko, S.I., 2016b. Ultrasound-assisted reductive dissolution of CeO_2 and PuO_2 in the presence of Ti particles. Dalton Trans., 2016, 45, 8802. https://doi.org/10.1039/c5dt04931h

Benzerga, A.A., Bréchet, Y., Needleman, A., Van der Giessen, E., 2005. The stored energy of cold work: Predictions from discrete dislocation plasticity. Acta Mater. 53, 4765–4779. https://doi.org/10.1016/j.actamat.2005.07.011

Blum, A., Lasaga, A., 1988. Role of surface speciation in the low-temperature dissolution of minerals. Nature 331, 431–433.

Blum, A.E., Yund, R.A., Lasaga, A.C., 1990. The effect of dislocation density on the dissolution rate of quartz. Geochim. Cosmochim. Acta 54, 283–297. https://doi.org/10.1016/0016-7037(90)90318-F

Bourges, J., Madic, C., Koehly, G., Lecomte, M., 1986. Dissolution of plutonium dioxide in nitric acid media by silver(II) electroreduction. J. -Common Met. 122 pp. 303–311.

Brueziere, J., Tribout-Maurizi, A., Durand, L., Bertrand, N., 2013. Polyvalent fuel treatment facility (TCP): shearing and dissolution of used fuel at La Hague facility. American Nuclear Society - ANS; La Grange Park (United States).

Burney, G.A., Smith, P.K., 1984. Controlled PuO/sub 2/particle size from Pu (III) oxalate precipitation. Du Pont de Nemours (EI) and Co., Aiken, SC (USA). Savannah River Lab.

Cerium Oxide Nanostructures and their Applications | IntechOpen https://www.intechopen.com/books/functionalized-nanomaterials/cerium-oxide-nanostructures-and-their-applications (accessed Apr 25, 2019)

Cheary, R.W., Coelho, A., 1992. A fundamental parameters approach to X-ray line-profile fitting. J. Appl. Crystallogr. 25, 109–121. https://doi.org/10.1107/S0021889891010804

Chen, H.-I., Chang, H.-Y., 2005. Synthesis and characterization of nanocrystalline cerium oxide powders by two-stage non-isothermal precipitation. Solid State Commun. 133, 593–598. https://doi.org/10.1016/j.ssc.2004.12.020

Claparede, L., Clavier, N., Dacheux, N., Mesbah, A., Martinez, J., Szenknect, S., Moisy, P., 2011a. Multiparametric Dissolution of Thorium–Cerium Dioxide Solid Solutions. Inorg. Chem. 50, 11702–11714. https://doi.org/10.1021/ic201699t

Claparede, L., Clavier, N., Dacheux, N., Moisy, P., Podor, R., Ravaux, J., 2011b. Influence of Crystallization State and Microstructure on the Chemical Durability of Cerium–Neodymium Mixed Oxides. Inorg. Chem. 50, 9059–9072. https://doi.org/10.1021/ic201269c

Claparede, L., Tocino, F., Szenknect, S., Mesbah, A., Clavier, N., Moisy, P., Dacheux, N., 2015. Dissolution of Th1−xUxO2: Effects of chemical composition and microstructure. J. Nucl. Mater. 457, 304–316. https://doi.org/10.1016/j.jnucmat.2014.11.094

Corkhill, C.L., Bailey, D.J., Tocino, F.Y., Stennett, M.C., Miller, J.A., Provis, J.L., Travis, K.P., Hyatt, N.C., 2016. Role of Microstructure and Surface Defects on the Dissolution Kinetics of CeO_2, a UO_2 Fuel Analogue. ACS Appl. Mater. Interfaces 8, 10562–10571. https://doi.org/10.1021/acsami.5b11323

Corkhill, C.L., Myllykylä, E., Bailey, D.J., Thornber, S.M., Qi, J., Maldonado, P., Stennett, M.C., Hamilton, A., Hyatt, N.C., 2014. Contribution of Energetically Reactive Surface Features to the Dissolution of CeO_2 and ThO_2 Analogues for Spent Nuclear Fuel Microstructures. ACS Appl. Mater. Interfaces 6, 12279–12289. https://doi.org/10.1021/am5018978

Dalodière, E., Virot, M., Moros ni, V. et al., 2017 Insights into the sonochemical synthesis and properties of salt-free intrinsic plutonium colloids. Sci Rep 7, 43514. https://doi.org/10.1038/srep43514

De Almeida, L., Grandjean, S., Vigier, N., Patisson, F., 2012. Insights into the thermal decomposition of lanthanide (III) and actinide (III) oxalates–from neodymium and cerium to plutonium. Eur. J. Inorg. Chem. 2012, 4986–4999.

Deshpande, S., Patil, S., Kuchibhatla, S.V., Seal, S., 2005. Size dependency variation in lattice parameter and valency states in nanocrystalline cerium oxide. Appl. Phys. Lett. 87, 133113. https://doi.org/10.1063/1.2061873

Fournier, S., 2000. Etude de la dissolution des oxydes mixtes (U,Pu)O2 à forte teneur en plutonium (thesis). Montpellier 2.

Goharshadi, E.K., Samiee, S., Nancarrow, P., 2011. Fabrication of cerium oxide nanoparticles: Characterization and optical properties. J. Colloid Interface Sci. 356, 473–480. https://doi.org/10.1016/j.jcis.2011.01.063

Goode, J.H., 1965. HOT-CELL DISSOLUTION OF HIGHLY IRRADIATED 20% PuO $ sub 2$-80% UO $ sub 2$ FAST-REACTOR FUEL SPECIMENS. Oak Ridge National Lab., Tenn.

Hailstone, R.K., DiFrancesco, A.G., Leong, J.G., Allston, T.D., Reed, K.J., 2009. A Study of Lattice Expansion in CeO2 Nanoparticles by Transmission Electron Microscopy. J. Phys. Chem. C 113, 15155–15159. https://doi.org/10.1021/jp903468m

Heintz, J., Bernier, J., 1986. SYNTHESIS AND SINTERING PROPERTIES OF CERIUM OXIDE POWDERS PREPARED FROM OXALATE PRECUSORS. J. Phys. Colloq. 47, C1-25-C1-29. https://doi.org/10.1051/jphyscol:1986104

Horlait, D., Claparede, L., Tocino, F., Clavier, N., Ravaux, J., Szenknect, S., Podor, R., Dacheux, N., 2014. Environmental SEM monitoring of Ce1−xLnxO2−x/2 mixed-oxide microstructural evolution during dissolution. J. Mater. Chem. A 2, 5193–5203. https://doi.org/10.1039/C3TA14623E

Horlait, D., Clavier, N., Szenknect, S., Dacheux, N., Dubois, V., 2012. Dissolution of Cerium(IV)–Lanthanide(III) Oxides: Comparative Effect of Chemical Composition, Temperature, and Acidity. Inorg. Chem. 51, 3868–3878. https://doi.org/10.1021/ic300071c

Hull, S., Norberg, S.T., Ahmed, I., Eriksson, S.G., Marrocchelli, D., Madden, P.A., 2009. Oxygen vacancy ordering within anion-deficient Ceria. J. Solid State Chem. 182, 2815–2821. https://doi.org/10.1016/j.jssc.2009.07.044

Joret, L., 1995. Influence d'un rayonnement microonde sur la cinetique de dissolution de uo2, ceo2 et co3o4 en milieu nitrique (thesis). Paris 6.

Katz, J.J., Seaborg, G.T., Morss, L.R., 1987. Chemistry of the actinide elements. Second edition.

Kim, H.S., Joung, C.Y., Lee, B.H., Oh, J.Y., Koo, Y.H., Heimgartner, P., 2008. Applicability of CeO2 as a surrogate for PuO2 in a MOX fuel development. J. Nucl. Mater. 378, 98–104. https://doi.org/10.1016/j.jnucmat.2008.05.003

Leblanc, M., Leturcq, G., Welcomme, E., Deschanels, X., Delahaye, T., 2019. Actinide mixed oxide conversion by advanced thermal denitration route. J. Nucl. Mater. 519, 157–165. https://doi.org/10.1016/j.jnucmat.2019.03.049

Lee, Y., He, G., Akey, A.J., Si, R., Flytzani-Stephanopoulos, M., Herman, I.P., 2011. Raman Analysis of Mode Softening in Nanoparticle CeO2−δ and Au-CeO2−δ during CO Oxidation. J. Am. Chem. Soc. 133, 12952–12955. https://doi.org/10.1021/ja2044479j

Ma, R., Jahurul Islam, M., Amaranatha Reddy, D., Kim, T.K., 2016. Transformation of CeO2 into a mixed phase CeO2/Ce2O3 nanohybrid by liquid phase pulsed laser ablation for enhanced photocatalytic activity through Z-scheme pattern. Ceram. Int. 42, 18495–18502. https://doi.org/10.1016/j.ceramint.2016.08.186

X. Machuron-Mandard, C. Madic, G. Koehly. Procédé de dissolution réductrice du Pu02, utilisable notamment pour le traitement de déchets organiques contaminés par Pu02, EP0312433A1, 1989. https://patents.google.com/patent/EP0312433A1/fr (accessed April 20, 2021).

Paier, J., Penschke, C., Sauer, J., 2013. Oxygen Defects and Surface Chemistry of Ceria: Quantum Chemical Studies Compared to Experiment. Chem. Rev. 113, 3949–3985. https://doi.org/10.1021/cr3004949

Park, S., Vohs, J.M., Gorte, R.J., 2000. Direct oxidation of hydrocarbons in a solid-oxide fuel cell. Nature 404, 265–267. https://doi.org/10.1038/35005040

Petříček, V., Dušek, M., Palatinus, L., 2014. Crystallographic Computing System JANA2006: General features. Z. Für Krist. - Cryst. Mater. 229, 345–352. https://doi.org/10.1515/zkri-2014-1737

Poinssot, C., Rostaing, C., Grenèche, S., Boullis, B., 2012. Recycling the Actinides, The Cornerstone of Any Sustainable Nuclear Fuel Cycles. Procedia Chem., ATALANTE 2012 International Conference on Nuclear Chemistry for Sustainable Fuel Cycles 7, 349–357. https://doi.org/10.1016/j.proche.2012.10.055

Rankin, D.T., Burney, G.A., 1975. Particle size of 238-Pu02 obtained by oxalate precipitation and calcination. Bull. Amer. Ceram. Soc 54, 1061–1065.

Scott Barney, G., 1977. The kinetics of plutonium oxide dissolution in nitric/hydrofluoric acid mixtures. J. Inorg. Nucl. Chem. 39, 1665–1669. https://doi.org/10.1016/0022-1902(77)80123-1

Skorodumova, N.V., Simak, S.I., Lundqvist, B.I., Abrikosov, I.A., Johansson, B., 2002. Quantum Origin of the Oxygen Storage Capability of Ceria. Phys. Rev. Lett. 89, 166601. https://doi.org/10.1103/PhysRevLett.89.166601

Spadaro, M.C., Luches, P., Bertoni, G., Grillo, V., Turner, S., Van Tendeloo, G., Valeri, S., D'Addato, S., 2016. Influence of defect distribution on the reducibility of CeO_{2-x} nanoparticles. Nanotechnology 27, 425705. https://doi.org/10.1088/0957-4484/27/42/425705

Spanier, J.E., Robinson, R.D., Zhang, F., Chan, S.-W., Herman, I.P., 2001. Size-dependent properties of ${\mathrm{CeO}}_{2\ensuremath{-}y}$ nanoparticles as studied by Raman scattering. Phys. Rev. B 64, 245407. https://doi.org/10.1103/PhysRevB.64.245407

Taylor, R., 2015. Reprocessing and Recycling of Spent Nuclear Fuel. Elsevier.

Tkáčová, K., Baláž, P., Mišura, B., Vigdergauz, V.E., Chanturiya, V.A., 1993. Selective leaching of zinc from mechanically activated complex Cu□Pb□Zn concentrate. Hydrometallurgy 33, 291–300. https://doi.org/10.1016/0304-386X(93)90068-O

Touron, E., Boullis, B., Chabert, C., 2016. Overview of fuel cycle perspective for France.

Tromans, D., Meech, J.A., 2001. Enhanced dissolution of minerals: stored energy, amorphism and mechanical activation. Miner. Eng. 14, 1359–1377. https://doi.org/10.1016/S0892-6875(01)00151-0

Tromans, D., Meech, J.A., 1999. Enhanced dissolution of minerals: Microtopography and mechanical activation. Miner. Eng. 12, 609–625. https://doi.org/10.1016/S0892-6875(99)00047-3

Trovarelli, A., 2002. Catalysis by Ceria and Related Materials, Catalytic Science Series. PUBLISHED BY IMPERIAL COLLEGE PRESS AND DISTRIBUTED BY WORLD SCIENTIFIC PUBLISHING CO. https://doi.org/10.1142/p249

Trovarelli, A., de Leitenburg, C., Boaro, M., Dolcetti, G., 1999. The utilization of ceria in industrial catalysis. Catal. Today 50, 353–367. https://doi.org/10.1016/S0920-5861(98)00515-X

Tsunekawa, S., Sahara, R., Kawazoe, Y., Kasuya, A., 2000. Origin of the Blue Shift in Ultraviolet Absorption Spectra of Nanocrystalline CeO_{2−<I>x</I>} Particles. Mater. Trans. JIM 41, 1104–1107. https://doi.org/10.2320/matertrans1989.41.1104

Tsunekawa, S., Sivamohan, R., Ohsuna, T., Takahashi, H., Tohji, K., 1999. Ultraviolet Absorption Spectra of CeO2 Nano-Particles [WWW Document]. Mater. Sci. Forum. https://doi.org/10.4028/www.scientific.net/MSF.315-317.439

Turner, S., Lazar, S., Freitag, B., Egoavil, R., Verbeeck, J., Put, S., Strauven, Y., Van Tendeloo, G., 2011. High resolution mapping of surface reduction in ceria nanoparticles. Nanoscale 3, 3385. https://doi.org/10.1039/c1nr10510h

Uriarte, A.L., Rainey, R.H., 1965. Dissolution of High-Density UO2, PuO2 and UO2-PuO2 Pellets in Inorganic Acids, Oak Ridge National Laboratory.

Vollath, D., Wedemeyer, H., Elbel, H., Günther, E., 1985. On the Dissolution of (U,Pu)O2 Solid Solutions with Different Plutonium Contents in Boiling Nitric Acid. Nucl. Technol. 71, 240–245. https://doi.org/10.13182/NT85-A33723

Younis, A., Chu, D., Li, S., 2016. Cerium Oxide Nanostructures and their Applications. Funct. Nanomater. https://doi.org/10.5772/65937

Zhang, F., Chan, S.-W., Spanier, J.E., Apak, E., Jin, Q., Robinson, R.D., Herman, I.P., 2002. Cerium oxide nanoparticles: Size-selective formation and structure analysis. Appl. Phys. Lett. 80, 127–129. https://doi.org/10.1063/1.1430502

Zhang, F., Jin, Q., Chan, S.-W., 2004a. Ceria nanoparticles: Size, size distribution, and shape. J. Appl. Phys. 95, 4319–4326. https://doi.org/10.1063/1.1667251

Zhang, F., Jin, Q., Chan, S.-W., 2004b. Ceria nanoparticles: Size, size distribution, and shape. J. Appl. Phys. 95, 4319–4326. https://doi.org/10.1063/1.1667251

Ziouane, Y., Milhau, T., Maubert, M., Arab-Chapelet, B., Leturcq, G., 2018. Dissolution kinetics of CeO2 powders with different morphologies and analogy to PuO2 dissolution. Hydrometallurgy 177, 205–213. https://doi.org/10.1016/j.hydromet.2018.03.016

Highlights

- High energy milling of ceria powders
- Structural and microstructural characterizations of milled ceria
- Dissolution of ceria powders in nitric acid 8.5M at 95°C
- Effect of oxygen vacancies and dislocation on dissolution kinetics